Through hydrogen spillover to fabricate novel 3DOM-HxWO₃/Pt/CdS Z-scheme heterojunctions for enhanced photocatalytic hydrogen evolution

Xiaoqing Yan[a], Baorong Xu[a], Xiaona Yang[a], Jinjia Wei[a], Bolun Yang[a], Lei Zhao[b], Guidong Yang[a],*

[a] XJTU-Oxford International Joint Laboratory for Catalysis, School of Chemical Engineering and Technology, Xi'an Jiaotong University, Xi'an, 710049, PR China
[b] School of Civil Engineering and Architecture, Xinxiang University, Xinxiang, 453003, PR China

ABSTRACT

The use of hydrogen spillover is considered to be a promising strategy to prepare H containing photocatalyst for enhanced hydrogen evolution performance. In this work, we for the first time employ the hydrogen spillover assisted by in-situ hydrothermal method to successfully synthesize the novel 3DOM-HxWO₃/Pt/CdS Z-scheme heterojunction. In this special photocatalytic system, three-dimensionally ordered macroporous (3DOM) structure provide a number of active sites for the mass transfer, and the Z-scheme architecture initiatively induce the electrons migration to achieve a high efficient charge separation. As a result, the as-prepared samples show a prominent apparent quantum efficiency (AQE) of 58.80% (420 nm) and excellent hydrogen production rate of 39.2 mmol g^{-1} h^{-1}, which is 13.5 times as high as that of the pure CdS (AQE of 23.15%). This work provides a new insight into the design and synthesis of porous Z-scheme heterojunction system with excellent solar light adsorption and highly-efficient charge spatial separation.

1. Introduction

As a promising energy source, the hydrogen has attracted much attention owing to its clean, cheap and high energy content, which thus has been vastly used to solving the global energy crisis and environmental pollution problem [1–4]. However, this ideal source still faces enormous challenge due to the fact that hydrogen was mainly produced from the un-reproducing resource of fossil fuel, while its production process is high energy consumption and non-environmental friendliness. Therefore, exploring a novel technology to economically and effectively produce H₂ is urgent [5–8].

Up to now, a number of studies have been proved that the solar-light driven water splitting by semiconductor photocatalyst is a promising technology for the hydrogen production [9–11]. Among various semiconductor photocatalysts, the novel hydrogen tungsten bronze (H$_x$WO₃) is considered to be an excellent candidate material due to its eco-friendliness, low-cost and good photostability [12,13]. More importantly, the synthesis procedure of tungsten bronzes (H$_x$WO₃) is very simple: under the hydrogen spillover conditions, the atomic H could migrate from precious metal to the WO₃ surface and further dope into the lattice of WO₃ to produce a turquoise H$_x$WO₃ material [14,15]. In addition, compared with WO₃, the HxWO₃ shows an amazing optical absorption property, which can harvest broad spectrum of solar light, from ultraviolet (UV) to near-infrared (NIR) region, leading to greatly

enhance the visible-light-induced catalytic activity of semiconductor [16]. However, a typical shortage of HxWO₃ limited its further practical application in the photocatalytic hydrogen evolution, that is, the conduction band potential of H$_x$WO₃ (0.7 eV) is more positive than that of water reduction potential (0.0 eV vs NHE) [17], resulting in the use of HxWO₃ to generate hydrogen still faces an extreme challenge.

Recently, a lot of reports have been proved that the construction of Z-scheme heterojunction is one of novel strategy to change the photo-induced electron migration path, making some semiconductor photocatalysts without original performance of H₂ production generate the activity of photocatalytic hydrogen evolution [18–21]. In our recent studies, we found that the HxWO₃ and CdS possess a much matched band structure, which are allowed to easily form the Z-scheme heterojunction between the interface of HxWO₃ and CdS. In the HxWO₃/CdS Z-scheme system, the photogenerated electrons on the conduction band (CB) of HxWO₃ can be captured by the holes on the valence band (VB) of CdS, while the photogenerated electrons of CdS and the holes of HxWO₃ remain on the original position with a lower (−0.52 eV) and higher band position (+3.1 eV), respectively. Thus, the spatially directional migration and separation of photogenerated electron–hole pairs in the Z-scheme system is significantly enhanced, and the Vis-NIR light absorption performance can be synchronously improved. As a result, the special Z-scheme properties would endow the HxWO₃/CdS heterojunction a better hydrogen production performance. In addition,

* Corresponding author.
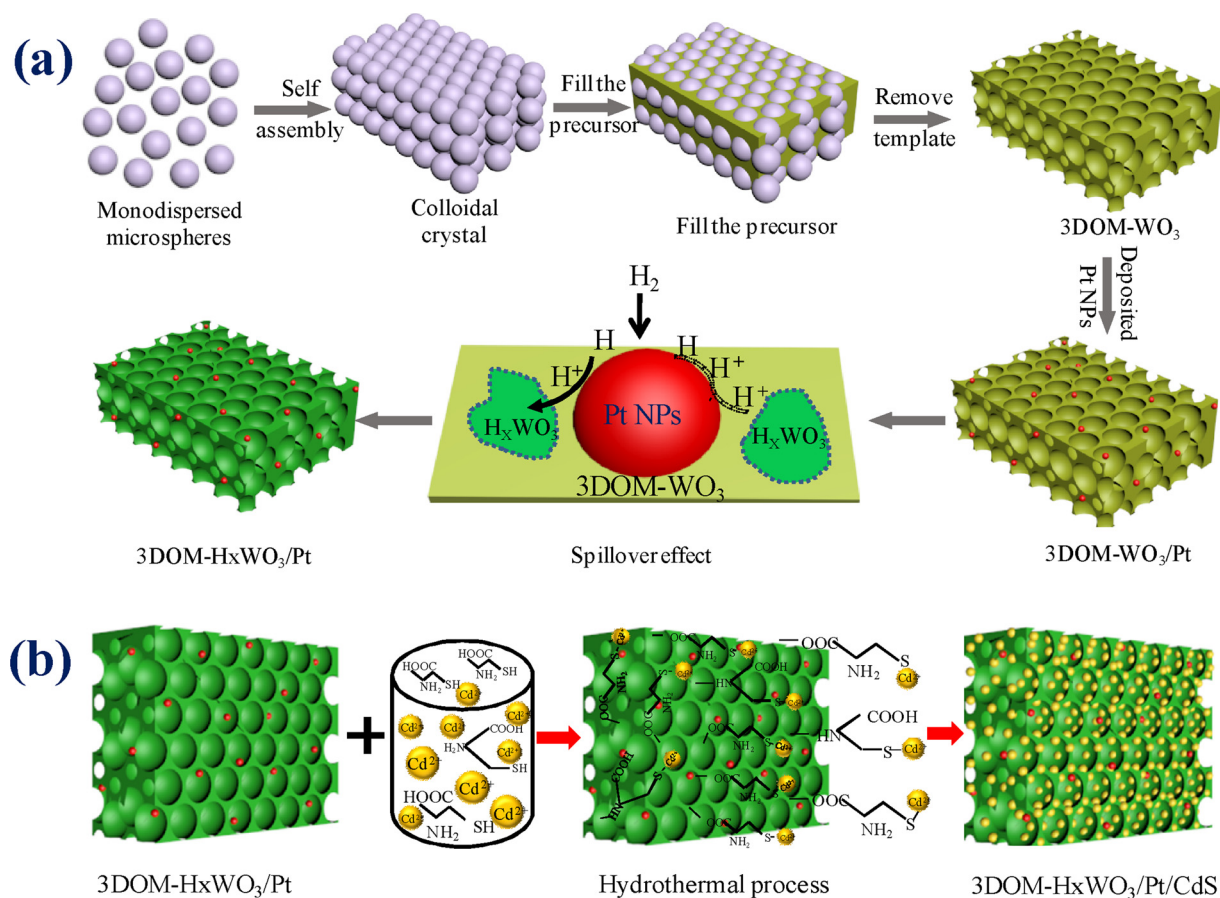 E-mail address: guidongyang@xjtu.edu.cn (G. Yang).

Fig. 1. (a) Formation route of 3DOM-HxWO$_3$/Pt, (b) Formation route of 3DOM-HxWO$_3$/Pt/CdS.

it is well know that the preparation of photocatalytic materials with the high specific surface area and excellent pore structure is a fascinating way to further improve the charge migration and mass transfer in photoreaction [22]. Therefore, to construct novel HxWO$_3$/CdS composites with porous nanostructures, especially with three-dimensionally ordered macroporous structure, may present a huge merit to significantly enhance the photocatalytic activity of the aforementioned Z-scheme heterojunction composites, because the high surface area and interconnected macroporous structure can supply a lot of reactive sites to facilitate the adsorption, mass diffusion and desorption of reactant during the photocatalytic reaction [23–25].

Inspired by above motivation, in this work, we for the first time synthesized the novel all-solid-state 3DOM-HxWO$_3$/Pt/CdS Z-scheme heterojunction through in situ growth of CdS NPs on the surface of 3DOM-HxWO$_3$/Pt for enhanced photocatalytic H$_2$ evolution activities. Under visible-light irradiation, the formation of 3DOM-HxWO$_3$/Pt/CdS composites show the excellent hydrogen production activity owing to the synergistic effects of optical absorption and spatial separation of photogenerated charges through the construction of Z-scheme heterojunction. The photocatalytic reaction mechanism as well as the electrons migration path in the Z-scheme heterojunction was proposed according to the characterization results. In this case, the high hydrogen production activity and unexceptionable solar absorption ability would endow the as-obtained 3DOM-HxWO$_3$/Pt/CdS photocatalyst a good engineering application potential.
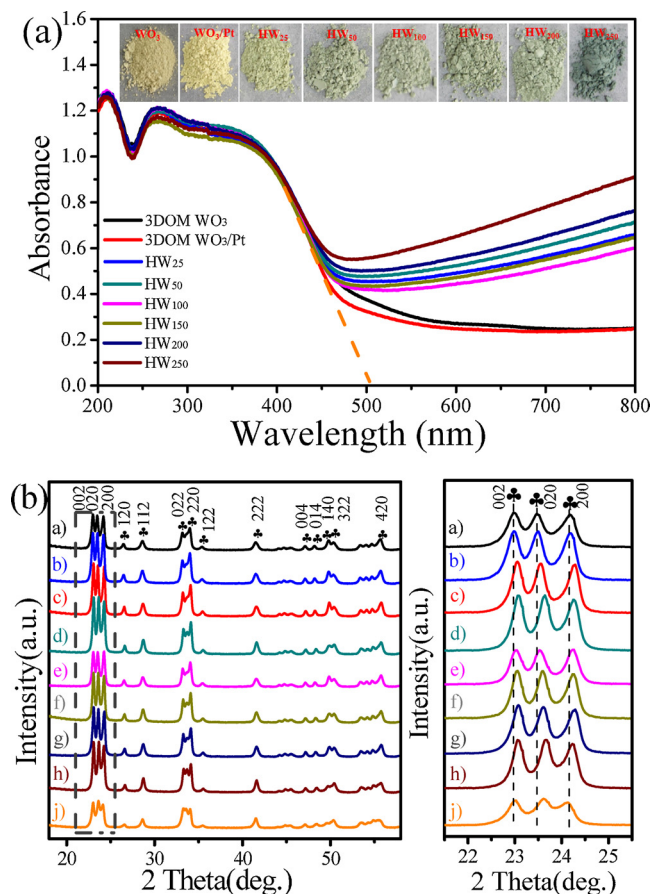
2. Experimental method

2.1. Preparation of highly ordered PS colloidal crystal microspheres

PS microspheres were prepared by a slightly modified emulsifier-free emulsion polymerization technique [26,27]. At first, 5.0 g PVP, 0.2 g AIBN and 140 mL absolute ethyl alcohol were adding into a three-necked, 250 mL round-bottomed flask. Secondly, 10 mL deionized water was adding after the mixed solution was completely dispersed under ultrasonication. Next, the water-cooling condenser was fixed to the flask and the shielding gas of nitrogen was bubbled to deaerate the mixture and the third necks were closed with a stopper. Then, keep constant stirring (400 rpm) and N$_2$ aerating, 12 g styrene was poured into the flask after the flask was heated to 70 °C by a water bath. After reacted at 70 °C for 24 h, the color of milk white PS colloidal crystal microspheres were obtained and were suspended in the mixed solution. When the solution cooled to room temperature, the PS-containing liquid was filtered and washed with ethanol and deionized water. Eventually, the solid block was completely dispersed again by ultrasonication in 90 mL deionized water. The suspended was centrifuged at 3000 rpm for 3 h and then the solid block was dried in centrifugal tubes at 60 °C by mean of dryer. So far, the arrayed highly ordered PS templates with 1000 nm colloidal crystal microspheres were obtained.

2.2. Preparation of 3DOM-WO$_3$

3DOM WO$_3$ was prepared by a PS-template strategy and its typical procedure is shown as follows: at first, 1.0 g tungstic acid and 0.8 mL ammonium hydroxide was dissolved into 40 mL deionized water. When the mixed solution becomes a transparent solution, 1.26 g surfactant of oxalic acid and 5 mL alcohol was added. Next, 4 g PS template (ca. 1000 nm in diameter) was soaked in the above mixed solution and then dried at 80 °C in the vacuum drying oven. Finally, the precursor-PS was calcined in air at a ramp of 1 °C/min from room temperature to 500 °C and kept at 500 °C for 3 h. After being cooled to room temperature, the pure 3DOM-WO$_3$ with 800 nm macropore was obtained.

Fig. 2. Effect of H-treated temperature on materials optical and physicochemical properties: (a) UV–vis diffuse reflectance spectra (DRS) of 3DOM-WO$_3$, 3DOM-WO$_3$/Pt and 3DOM-H$_x$WO$_3$/Pt samples, the inset are the optical photograph of the samples. (b) XRD patterns of a) 3DOM-WO$_3$, b) 3DOM-WO$_3$/Pt, c) HW$_{25}$, d) HW$_{50}$, e) HW$_{100}$, f) HW$_{150}$, g) HW$_{200}$, h) HW$_{250}$, j) 3DOM-H$_x$WO$_3$/Pt-300 °C, respectively. The inset shows the magnification of the diffraction peak from 2θ value of 22° to 25°.

2.3. Preparation of 3DOM-WO$_3$/Pt

3DOM-WO$_3$/Pt was obtained by in-situ photodeposited strategy. 0.5 g 3DOM-WO$_3$ was dispersed in a mixture of solution (2 mL lactic acid, 40 mL deionized water, and 0.4 mL 1 wt.% H$_2$PtCl$_6$). When the solution was irradiated by 300 W xenon lamp for 3 h, the Pt nanoparticles would be in-situ anchored on the surface of 3DOM-WO$_3$. And after centrifuging and washing with deionized water, the sample of 3DOM-WO$_3$/Pt was obtained when the precipitant was dried at 60 °C for 12 h and calcined at 500 °C for 0.5 h, respectively.

2.4. Preparation of 3DOM-H$_x$WO$_3$/Pt

Tungsten bronzes (H$_x$WO$_3$) can be easy formed via the process of hydrogen spillover [14]. The detail procedure was described as follows: In the quartz tube, 0.1500 g 3DOM-WO$_3$/Pt was put in the middle area of tube furnace. Then, the H$_2$ gas was filled on the tube and it was keeping unchanged (100 mL/min). Next, the tube furnace was turn on and reached to the desired temperatures within 30 min. And the following step was calcined at desired temperatures for 20 min. The final, the carrying gases were continuous keeping 120 min in the process of cooling. The samples prepared with different temperature of 25 °C, 50 °C, 100 °C, 150 °C, 200 °C and 250 °C were denoted as HW$_{25}$, HW$_{50}$, HW$_{100}$, HW$_{150}$, HW$_{200}$, and HW$_{250}$, respectively.

2.5. Preparation of CdS/Pt

The CdS/Pt sample was prepared by in-situ photodeposited strategy. 0.5 g CdS was dispersed in a mixture of solution (2 mL lactic acid, 40 mL deionized water, and 0.4 mL 1 wt.% H$_2$PtCl$_6$). When the solution was irradiated by a 300 W xenon lamp for 3 h, the Pt nanoparticles would be in-situ anchored on the surface of CdS. And after centrifuging and washing with deionized water, the CdS/Pt sample can be obtained after the precipitant was dried at 60 °C for 12 h.

2.6. Synthesis of 3DOM-H$_x$WO$_3$/Pt/CdS Z-scheme heterojunction

The ternary 3DOM-H$_x$WO$_3$/Pt/CdS nanocomposite was prepared by a in-situ hydrothermal method. In this procedure, by using trifunctional surface modifiers (L-Cysteine), the ions Cd^{2+} can link onto the 3DOM-H$_x$WO$_3$/Pt surface [29–31]. In particular, 0.0580 g (~0.25 mmol) of 3DOM-HxWO$_3$, 0.2314 g (~0.75 mmol) of Cd(NO$_3$)$_2$ and 0.1212 g (~1 mmol) of L-Cysteine are mixed in 30 mL deionized water. After continuously stirring 12 h, 10 mL solution with 0.2700 g (1.125 mmol) Na$_2$S was injected into above solution. Next, the mixed solution was transferred into 50 mL Teflon-lined stainless-steel autoclave and heated at 110 °C for 2 h. After washing with ethanol and deionized water for three times, the precipitant was dried at 60 °C to finally obtain 3DOM-H$_x$WO$_3$/Pt/CdS Z-scheme heterojunction. For comparison, under the same condition, the HW$_{100}$ sample with different mole ratio CdS were prepared (the molar ratio are 1:1, 1:2, 1:3 and 1:4), and the SEM images as shown in Fig. S1. In addition, the CdS NPs loading on the HW$_{25}$, HW$_{50}$, HW$_{100}$, HW$_{150}$, HW$_{200}$, and HW$_{250}$, were also achieved, and those samples were denoted as CHW$_{25}$, CHW$_{50}$, CHW$_{100}$, CHW$_{150}$, CHW$_{200}$ and CHW$_{250}$, respectively (the SEM images as shown in Fig. S2).

2.7. Characterizations method

The crystal phases of all the as-prepared photocatalysts were observed by SHIMADZU Lab X XRD-6100, and the 2θ range was scanned from 10° to 80° with 10° min^{-1}. The surface morphology and microstructure of the samples were tested by the transmission microscopy (TEM, JEOL, JEM-2100) and the field-emission scanning electron microscope (SEM, JEOL, JSM-6700 F) equipped with the energy dispersive spectrometer (EDX), respectively. And the optical adoption properties of all samples were recorded by UV–vis diffuse reflection spectra (UV–vis DRS, SHIMADZU, UV-2600). The photoluminescence (PL) spectra were examined by a FLS980 fluorescence spectrophotometer (Edinburgh instruments) excited at 325 nm or 375 nm. And the specific surface area and pore size distribution plots were tested by BET and BJH method (BET, BELsorp). In addition, the X-ray photoelectron spectroscopy (XPS) was investigated by Kratos AXIS Ultra Dld photoelectron spectrometer with monochromatic Al-Kα excitation (hν = 1486.69 eV).

2.8. Electrochemical measurement

The transient photocurrent response and electrochemical impedance spectroscopy (EIS) were carried out by using an electrochemical station (PMC-2000A, AMETEK) in a standard three-electrode system. The working electrode coated with samples were prepared as follows: the sample (3 mg) was ultrasound dispersed evenly in deionized water (1 mL) with a 3 wt% Nafion solution, and then the mixed solution (10 μL) was spread onto the working electrode. At final, the working electrode was dried naturally. In this tested system of photocurrent and EIS measurements, an electrode coated with samples, an Ag/AgCl electrode and a platinum wire were chosen as working electrodes, reference electrode, and the counter electrode, respectively. A 1 M Na$_2$SO$_4$ aqueous solution was used as the electrolyte. In addition, it should be noted that the bias acted as an externally driving force can
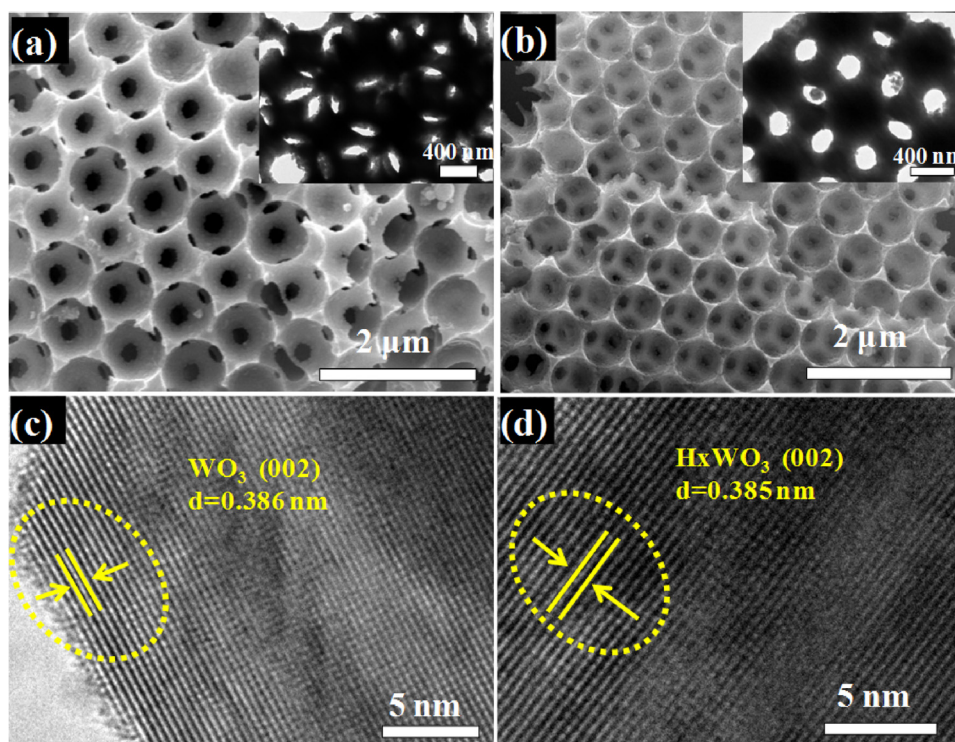
Fig. 3. SEM images (a–b), TME image (insets of a–b) and HRTEM (c–d) of 3DOM-WO$_3$ and HW$_{100}$ sample, respectively.
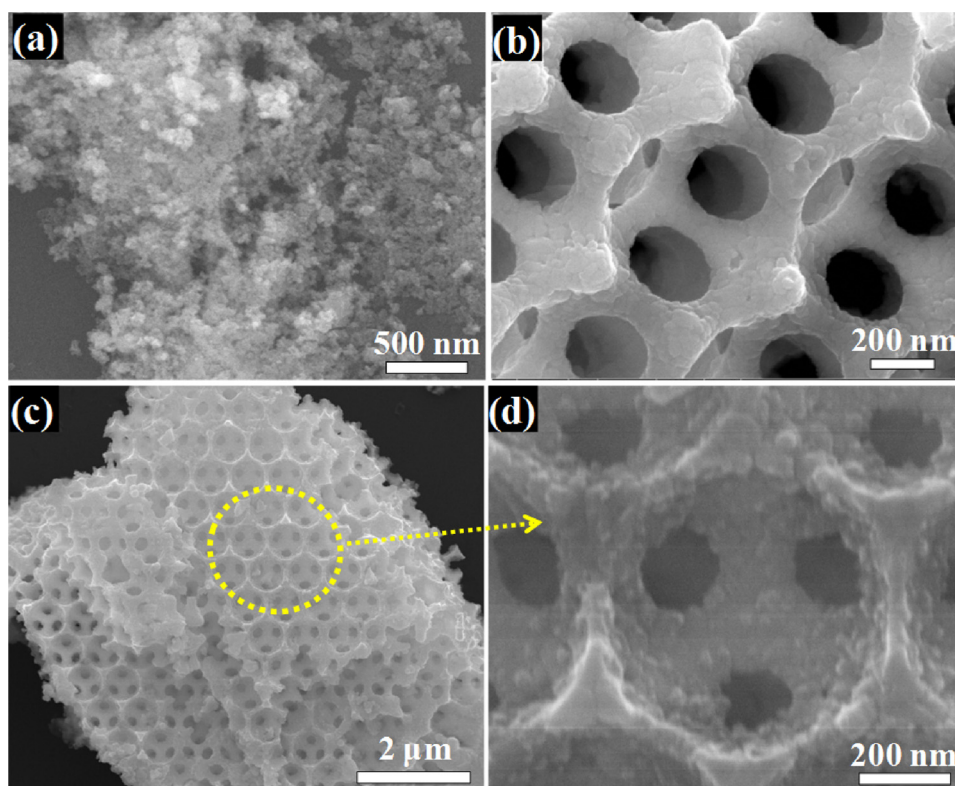

Fig. 4. SEM images of the obtained samples: (a) the pure CdS nanoparticles, (b) the HW$_{100}$ sample, (c–d) the CHW$_{100}$ sample.

promote the separation of photogenerated electron-hole pairs to obtain stable and obvious photoelectric signal [28], and the appropriate applied bias of 0.3 V vs. open-circuit voltage was thus chose.

2.9. Photocatalytic hydrogen evolution

The photocatalytic H$_2$ production reaction from water were carried out in a Pyrex reaction cell. Typically, 10 mg photocatalyst was dispersed in 60 mL aqueous solutions containing 10 mL lactic acid as a
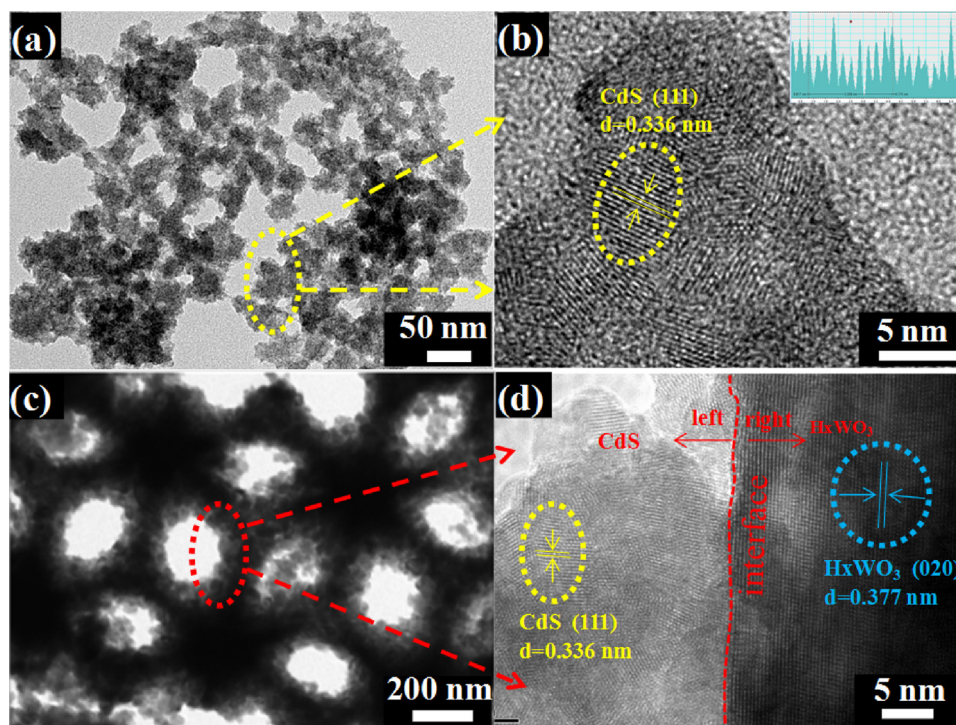
Fig. 5. TEM images of the obtained samples: (a–b) pure CdS nanoparticles, (c–d) CHW_{100} sample.

sacrificial electron donor. The solution was degassed with highly pure N_2 for 10 min to remove the O_2 in the reaction cell and then irradiated under visible-light (> 420 nm) at room temperature. Finally, the amount of H_2 production was analyzed by gas chromatography (Beifen-Ruili, SP-2100A, China).

The apparent quantum efficiency (AQE) of photocatalytic H_2 production was tested under the similar conditions. A Xe lamp (300 W), as the light source, was equipped with a 420 nm, 435 nm, 475 nm and 550 nm bandpass filter, respectively. The amount of H_2 evolution was counted after reacted for 3 h. the AQE for H_2 evolution was calculated according to the following equation [10,32]

$$AQE(\%) = \frac{\text{Number of reactor electrons}}{\text{Number of incident photons} \times 100} \times 100\%$$
$$= \frac{2 \times \text{Number of evolved hydrogen molecules}}{\text{Number of incident photons} \times 100} \times 100\%$$

3. Results and discussion

3.1. Effect of hydrogen spillover on the physicochemical properties of 3DOM-WO₃/Pt
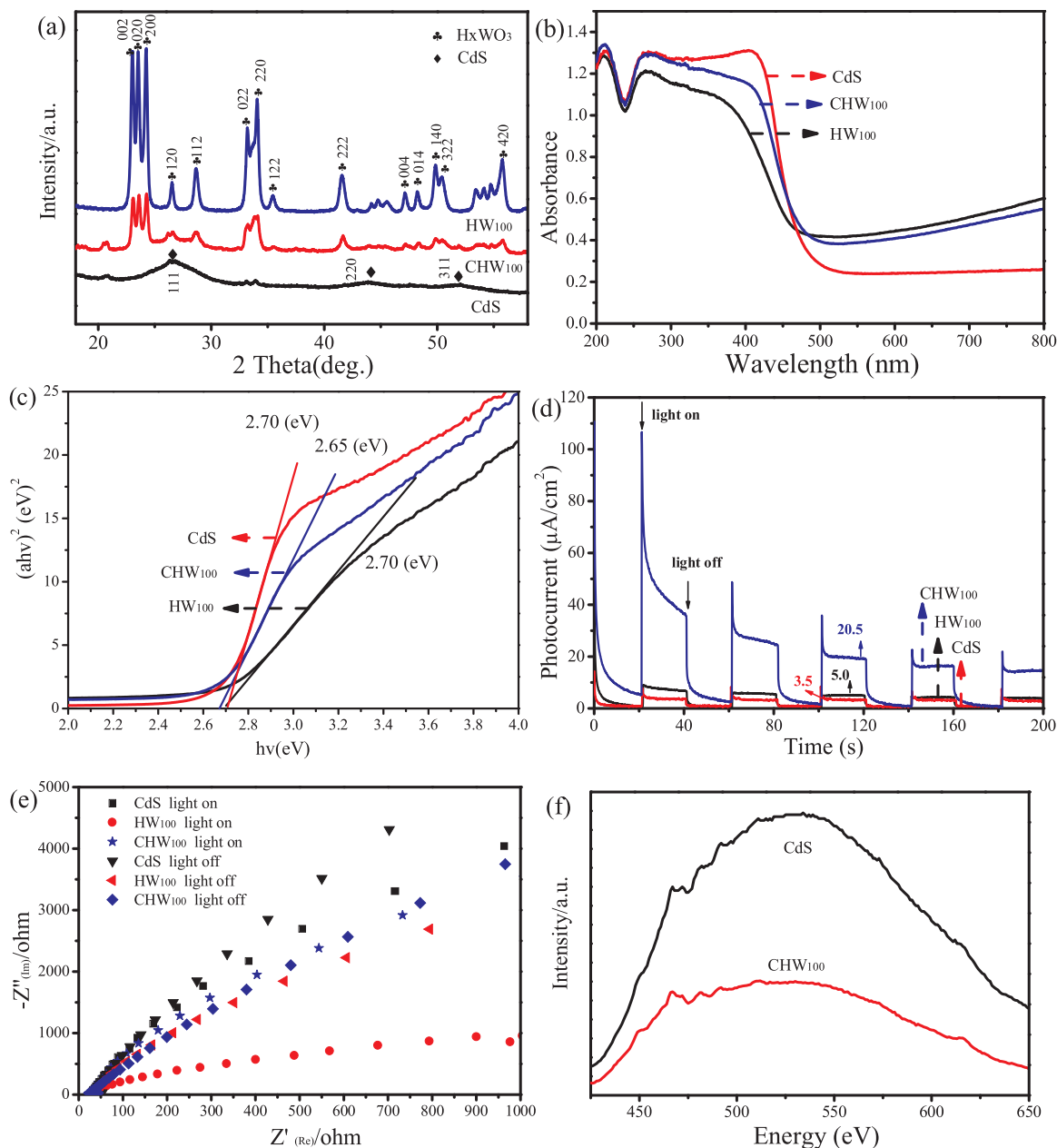
Colloidal crystal-templating method assisted by hydrothermal process is an effective way to prepare the Z-scheme heterojunction [33–35]. Fig. 1a shows the schematic diagram for the synthesis of 3DOM-HxWO₃ samples. As can be seen that the monodisperse PS microspheres are firstly obtained by the emulsifier-free emulsion polymerization technique, and then these monodisperse PS microspheres can be easily self-assembled 3D ordered colloidal crystal template when the solution was centrifuged at 3000 r/min for 3 h. Next, the precursor solution of WO₃ was immersed into the gap of these PS templates in vacuum oven at 80 °C for 12 h. After calcination, the 3DOM-WO₃ materials are obtained. Thirdly, the 3DOM-WO₃/Pt intermediate sample can be quickly formed via loading numerous highly dispersed Pt nanoparticles (NPs) on the surface of 3DOM-WO₃ under photo-deposited conditions. Lastly, the final 3DOM-HxWO₃/Pt samples are produced based on the hydrogen spillover process through calcining the 3DOM-

WO₃/Pt at different temperature annealing (25 °C to 250 °C) in the H_2 atmosphere for 20 min.

In-situ synthesis of CdS NPs on the 3DOM-HₓWO₃/Pt surface was carried out via the hydrothermal process as shown in Fig. 1b. First, the 3DOM-HxWO₃/Pt and the L-cysteine were added into the 30 mL deionized water with continually stirring for 5 h. And the metallic Cd^{2+} ions were then added into the above reactive system, which would be linked with L-cysteine and loaded on the skeletons of 3DOM materials. Because of the L-Cysteine as a bifunctional surface modifier for the formation of HS-R-COOH link between Cd^{2+} and WO₃ [30,31], when the Na₂S was added, the CdS nanoparticles would be in-situ anchored on the surface of 3DOM-HxWO₃/Pt. And then, the mixed solution was transferred into Teflon-lined stainless-steel autoclave and heated at 110 °C for 2 h. After centrifugalizing and washing with ethanol and deionized water for three times, the resulting precipitant was dried by vacuum freeze dryer to finally obtain the 3DOM-HxWO₃/Pt/CdS heterojunction.

Fig. 2a shows the UV–vis diffuse reflectance spectra (DRS) and the color change of the as-prepared samples. It can be seen from the inset of Fig. 2a that the pristine 3DOM WO₃ and 3DOM WO₃/Pt is yellow in color. However, when the 3DOM-WO₃/Pt was calcined by different annealing temperature (25 °C to 250 °C) in H_2 atmosphere, its color is changed gradually from light green (25 °C) to deep green (250 °C). This phenomenon indicates that the possible phase change and/or modification are occurred in the crystal structure of WO₃ during hydrogen treatment [36]. In the UV–vis diffuse reflectance spectra (DRS), all the samples show the same and high absorbance in the UV and visible light region below the wavelength of 500 nm. In additon, a very broad and slightly raised absorption tail that extends across the visible light region down to the NIR can be observed for these as-obtained samples, indicating that the atomic of H has been successfully embedded in the lattice of WO₃ and the 3DOM-HxWO₃ is thus formed.

The X-ray diffraction (XRD) can give the detailed information about the crystal phase for the 3DOM-HxWO₃/Pt samples. In Fig. 2b, serval characteristic peaks can be clearly detected in the XRD data of pure 3DOM-WO₃ and 3DOM-WO₃/Pt at 22.98°, 23.48°, 24.18°, 26.43°, 28.58°, 33.17° and 34.00°, corresponding to the (002), (020), (200),

Fig. 6. (a) XRD patterns, (b) UV–vis diffuse reflectance spectra (DRS), (c) plots of (ahv)^2 versus energy (hv), (d) Transient photocurrent density, (e) electrochemical impedance spectroscopy (EIS) Nyquist plots (f) PL spectra of the samples of pure CdS NPs, HW$_{100}$ and CHW$_{100}$.

(120), (112), (022) and (220) diffraction plane of the orthorhombic structure WO$_3$ (JCPDS Card No. 71-0131). And the as-obtained 3DOM-H$_x$WO$_3$/Pt sample shows a similar XRD profile with 3DOM-WO$_3$ and 3DOM-WO$_3$/Pt. However, a careful inspection of the main diffraction peaks (002, 020 and 200 facets in the inset of Fig. 2b) reveal that the peak positions of 3DOM-H$_x$WO$_3$ shift slightly toward a higher 2θ value with the increase of H$_2$ treatment temperature. According to the previous report [37,38], the HW$_{100}$ sample shows the lattice distances of 0.3856, 0.3777 and 0.3665 nm for (002), (020) and (200) facets, respectively, which is slight difference with the corresponding (002), (020) and (200) facet values of 0.3867, 0.3786 and 0.3667 nm for WO$_3$. This phenomenon further confirmed that the atomic H has been successfully embedded in the lattice of WO$_3$ to form H$_x$WO$_3$. Moreover, no obvious characteristics peaks of Pt are observed due to its very low loading concentration.

In order to further observe the morphology change of 3DOM-WO$_3$/Pt sample before and after hydrogen spillover treatment, the 3DOM-WO$_3$ and HW$_{100}$ sample were tested by SEM and TEM, respectively. As shown in Fig. 3a–b, the pure 3DOM-WO$_3$ and HW$_{100}$ samples exhibit the typical opals structure, both of which have a periodicity 3D-interconnected walls and well-defined macroporous networks. The insets of Fig. 3a–b show the TEM images of 3DOM-WO$_3$ and HW$_{100}$ sample, respectively. It can be seen that the two samples present macroporous structure with diameters of about 800–1000 nm, and no significant difference was found in the microstructure, indicating that the process of photo-deposition Pt and treatment by H$_2$ gas was not given rise to the collapse of 3DOM morphologies. However, from the HRTEM image (Fig. 3c and d), the lattice spacing of HW$_{100}$ is 0.385 nm, which shift slightly when compared with the 3DOM-WO$_3$ (0.386 nm), this phenomenon is in agreement with the XRD data, suggesting that the atomic H had been successfully injected into WO$_3$ lattice.

Fig. S3a shows the photocurrent density of 3DOM-WO$_3$, 3DOM-WO$_3$/Pt and H-treated 3DOM-H$_x$WO$_3$/Pt samples. Compared with 3DOM-WO$_3$ and 3DOM-WO$_3$/Pt, the photon-to-electron conversion
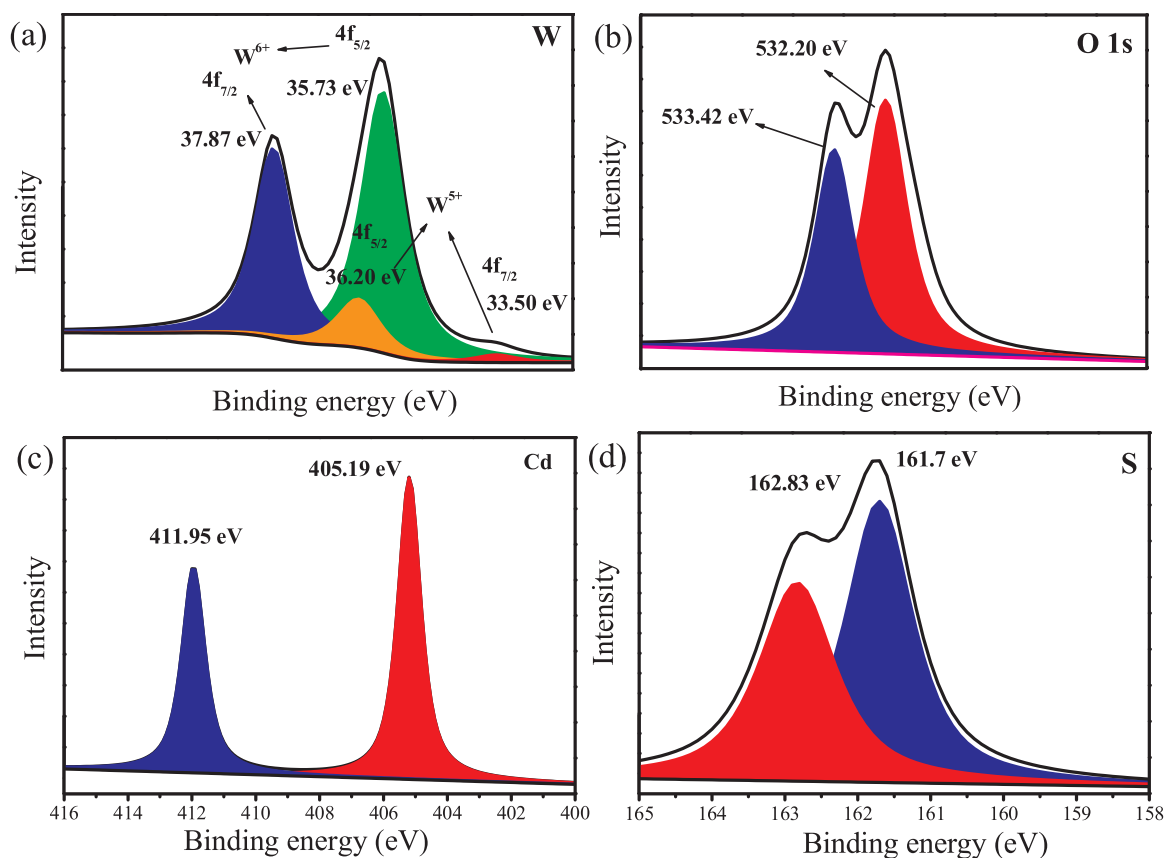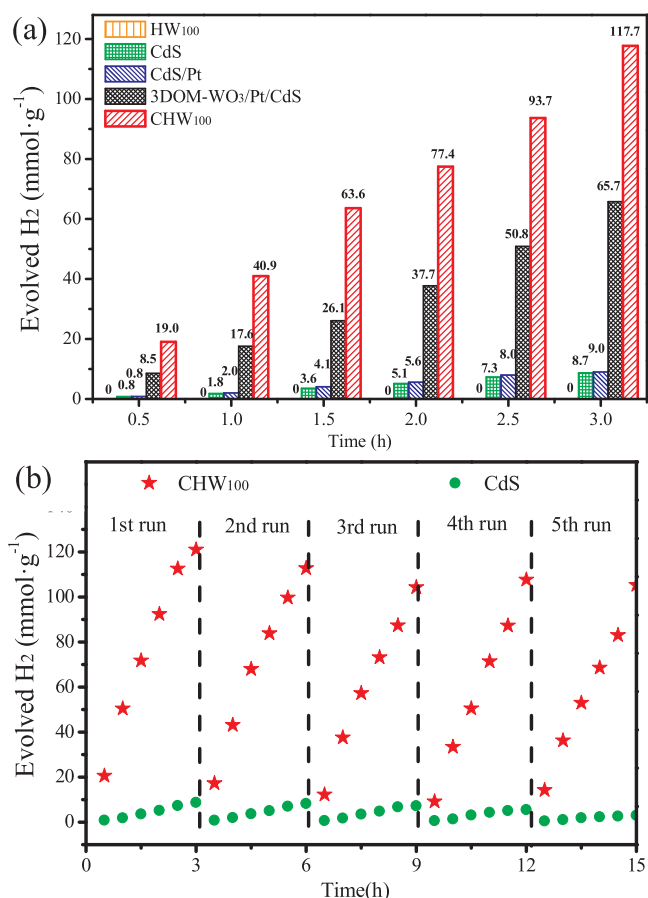
Fig. 7. XPS spectra of the CHW$_{100}$ sample, W 4f (a), O 1s (b) Cd 3d (c) and S 2p (d).

efficiency for the H-treated 3DOM-HxWO$_3$/Pt samples was obviously increased. Especially, the HW$_{100}$ sample exhibits the strongest photocurrent response signals (about 5.0 μA cm^{-2}), which is 10 times as high as that of the pristine 3DOM-WO$_3$ (about 0.5 μA cm^{-2}). However, in comparasion with the HW$_{100}$ sample, by increasing or decreasing the treatment temperature in H$_2$ atmosphere, the photocurrent density for these as-formed H-treated 3DOM-WO$_3$/Pt samples are more or less decreased. In addition, when the Xe lamp (300 W) were respectively equipped with the 435 nm, 475 nm, 550 nm and 700 nm band-pass filter to irradiate the as-obtained samples, the photocurrent response signals of 3DOM-WO$_3$, 3DOM-WO$_3$/Pt and HW$_{100}$ samples are quite different. From Fig. S3b–e, it is seen that the 3DOM-WO$_3$ and 3DOM-WO$_3$/Pt samples only show weak photocurrent response signals due to its corresponding bandgap of 2.70 eV, which just can be excited by the light below wavelength of 459 nm. However, the HW$_{100}$ sample shows the strongest photocurrent response signals, even it was irradiated by the long-wavelength light (550 nm or 700 nm), indicating that the sample has outstanding charge excitation ability in the wide light response region, which is in accordance with the UV–vis diffuse reflectance spectra. For the electrochemical impedance spectroscopy (EIS) Nyquist plots, the diameter of the Nyquist circle of HW$_{100}$ (Fig. S3f) is much smaller than that of pure 3DOM-WO$_3$, 3DOM-WO$_3$/Pt and other 3DOM-HxWO$_3$/Pt samples, demonstrating that the H-treated 3DOM-WO$_3$/Pt sample prepared at 100 °C possesses ultrahigh electron conductivity and mobility [39,40]. In addition, the photoluminescence (PL) spectra were used to further evaluate the separation efficiency of electron–hole pairs (Fig. S4), in the case of 3DOM-WO$_3$/Pt and 3DOM-WO$_3$, it is showed that both of them have an intense PL emission peak at 473 nm (the excitation wavelength is 325 nm), suggesting that the two materials possess high recombination ability of electron–hole pairs. However, after annealing 3DOM-WO$_3$/Pt sample in H$_2$ atmosphere (especially for the HW$_{100}$ sample), the corresponding intensity of PL

emission peak showed a distinct weakening trend, indicating that the separation of electron-hole pairs and charge directional transfer in the samples is significantly enhanced when the atomic H was embed into WO$_3$ lattice. Interestingly, the HW$_{250}$ sample shows the strongest PL emission peak due to the formation of substoichiometric WO$_{3-x}$ after hydrogen treatment at 250 °C or above higher temperature, which can cause the high recombination of charges [36].

3.2. Effect of Z-scheme heterojunction on the photocatalytic hydrogen evolution of 3DOM-HxWO$_3$/Pt/CdS

According to the above results, it is seen that when the 3DOM-WO$_3$/Pt was treated at 100 °C in the H$_2$ atmosphere, the obtained sample (HW$_{100}$) has stronger visible light absorption, excellent photoelectric performance, ultrahigh electron conductivity and incredible photon-generated charge carriers production ability, all of which indicate that the HW$_{100}$ sample can be acted as the best support for the CdS loading to prepare the 3DOM-HxWO$_3$/Pt/CdS Z-scheme heterojunction (CHW$_{100}$). Fig. 4 shows the SEM images of pure CdS, HW$_{100}$ and CHW$_{100}$ samples. As can be seen from Fig. 4a, the pure CdS displays a representative aggregate structure, which is composed of numerous nanoparticles. In Fig. 4b, the HW$_{100}$ sample exhibits smooth and interpenetrating macroporous structure with diameters of about 1000 nm, which can provide a number of sites for the loading of CdS NPs on their 3DOM skeleton surface. So, in Fig. 4c–d, it can be clearly found that many tiny CdS NPs with diameter of about 50 nm were evenly distributed on the 3DOM skeletons of HW$_{100}$ sample. In addition, from the TEM images (Fig. 5a and c), it was further observed that the pure CdS samples possess typical nanoparticle morphology and uniformly loaded on the surface of 3DOM-HxWO$_3$, which are agreement with the SEM images and elemental mapping spectrum (Figure S5). In the HRTEM image (Fig. 5b), the lattice spacing (d values) of pure

Fig. 8. Effect of Z-scheme structure on photocatalytic H_2 evolution: (a) plots of photocatalytic H_2 evolution amount vs. irradiation time. (b) recycling H_2 evolution curve of CdS and CHW_{100} for 5 runs. Experimental conditions: photocatalyst 10 mg, deionized water 50 mL, lactic acid 10 mL and assisted by continuous stirring.
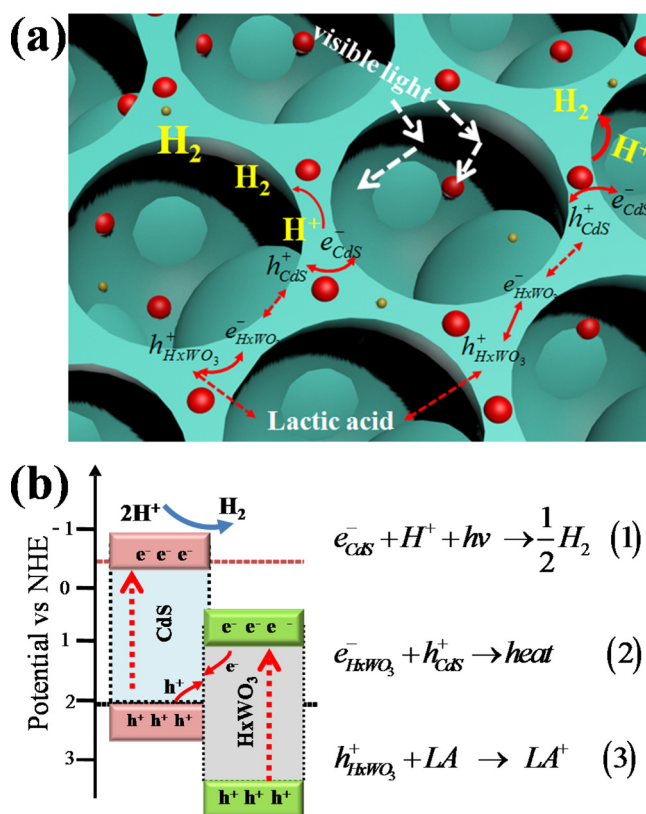

Fig. 9. Scheme illustrating the principle of charges transfer at the interface of 3DOM-HxWO$_3$/Pt/CdS Z-scheme heterojunction.

Table 1
the apparent quantum efficiency of pure CdS and CHW_{100} samples.

samples	420 nm	435 nm	475nm	550 nm
CdS	23.15%	19.70%	4.21%	0
CHW_{100}	58.80%	53.75%	18.55%	0

CdS NPs is estimated to be 0.336 nm, well agreeing with that of the (111) plane of the CdS sample (JCPDS Card No. 89-0440). In Fig. 5d, the d value of CHW_{100} was measured to be 0.377 nm, which is very close to the (020) plane of HxWO$_3$. Besides, the obvious interface contact was observed between 3DOM-HxWO$_3$ and CdS NPs, indicating that the CdS NPs are tightly grew on the skeleton surface of the HW_{100} sample, and thus a number of junctions between 3DOM-HxWO$_3$ and CdS can be formed, which could accelerate the photogenerated charge to migrate and separate.

Fig. 6a shows the XRD patterns of CHW_{100} together with the pure CdS and HW_{100} samples. The as-prepared HW_{100} and CHW_{100} exhibit similar X-ray diffraction data, this is because the HxWO$_3$ sample has the high crystallinity and the partial CdS XRD peaks were thus shielded. However, several weak peaks at 26.46°, 43.89° and 51.98° in the XRD pattern of CHW_{100} samples still are observed, which can be ascribed to the (111), (220) and (311) crystal planes of CdS, respectively (JCPDS No. 89-0440), indicating that the CHW_{100} sample is consisted of HxWO$_3$ and CdS, and no other impure peaks can be observed.

Fig. 6b shows the UV–vis diffuse reflectance spectra of the pure CdS, HW_{100} and CHW_{100} samples. In comparison with HW_{100} and CdS, the

CHW_{100} sample shows much stronger absorbance in the range of visible region below 500 nm, and the CHW_{100} sample also exhibits excellent light harvesting in the red or NIR region. In Fig. 6c, it can be observed that the three samples have different absorption edge, and their bandgap are about 2.70 eV of HW_{100}, 2.65 eV of CHW_{100} and 2.70 eV of CdS, respectively, which inferred by the transformed Kubelka-Munk function[21]. As shown in Fig. 6d, it is not surprise that the CHW_{100} presents the strongest photocurrent response signals (about 20.5 μA cm^{-2}), which is 4.1 times and 5.9 times as high as that of the HW_{100} (about 5.0 μA cm^{-2}) and pure CdS (about 3.5 μA cm^{-2}), respectively. Fig. 6e shows the EIS Nyquist plots of the CdS, HW_{100} and CHW_{100} under the situation of light on and light off, respectively. It can be seen that the diameter of the Nyquist circle of CHW_{100} is much smaller than that of pure CdS. This proved that the CHW_{100} samples has ultrahigh electron conductivity and mobility [21], which would lead to a faster interfacial charge transfer at the interface of CdS and HxWO$_3$ along Z-scheme pathway. Interestingly, the HW_{100} shows the smallest arc radius on the EIS Nyquist plots in the two cases of light on and light off, indicating that the 3DOM-WO$_3$/Pt treated by hydrogen has much better electron mobility among these samples. However, the HW_{100} with poor photocurrent response ability and low interfacial charge separation efficiency significantly limited the enhancement of photocatalytic activity. In Fig. 6f, the CHW_{100} sample shows the lowest PL emission peak at the wavelength of 534 nm when the sample was excited by the wavelength of 375 nm, suggesting that the CHW_{100} possesses the low recombination ability of photoexcited electron–hole pairs because the Z-scheme heterojunction structure provide a new path for the electrons migration, which will be discussed later.

To further examine the chemical components and electronic sates of elements in the CHW_{100} sample, the X-ray photoelectron spectroscopy (XPS) measurement was performed. In Fig. 7a, it is clearly found that two peaks located at the high binding energies of 37.87 eV and 35.73 eV, which can be assigned to W 4f$_{7/2}$ and W 4f$_{5/2}$, respectively,

derived from W^{6+} in HxWO3. In the meanwhile, the fitting results show that there are another two peaks appeared at the low binding energies of 36.20 eV and 33.50 eV, which can be respectively indexed to W $4f_{5/2}$ and W $4f_{7/2}$ from W^{5+} [41], indicating that the oxygen in WO3 is replaced by atomic H to form new tungsten oxidation state. In Fig. 7b, the peak of O 1s at the binding energy of 530.42 eV was characteristic of the lattice oxygen in HxWO3. And the peak located at 532.2 eV was assigned to the hydroxyl (O–H), indicating that the atomic H is linked by the atomic O in the formation of tungsten bronze [36]. The high resolution XPS spectrum of Cd 3d shows two peaks at 405.19 eV and 411.95 eV, which are assigned to Cd $3d_{5/2}$ and Cd $3d_{3/2}$ in CdS, respectively (Fig. 7c) [42]. As shown in Fig. 7d, two peaks of S $2p_{3/2}$ and S $2p_{1/2}$ located at the binding energy of 162.83 eV and 161.7 eV can be attributed to the presence of S^{2+} in CdS. No characteristics peak of Pt was found due to its very low loading concentration.

The N2 adsorption-desorption isotherm and the pore size distribution curve of the pure CdS, HW100 and CHW100 samples were shown in Fig. S6. And all the curves show the typical type-IV isotherm with H3 hysteresis loops according to the IUPAC classification [43], indicating that mesoporous structure has been produced in those samples. In addition, the existence of mesoporous structure can be also verified by the pore size distribution curves. Table S1 summarized the texture parameters of the pure CdS, HW100 and CHW100 samples, respectively. And the CHW100 sample shows the highest BET surface area of 138 m^2/g than that of pure CdS NPs (93 m^2/g) and HW100 (18 m^2/g), which displays that the 3DOM-HxWO3 with well-defined 3D-interconnected macroporous networks not only can provide a large number of sites for the loading of CdS NPs, but also favor the photogenerated electron transfer and reactant adsorption, as result of leading to the enhancement of photocatalytic activity.

In order to evaluate the photocatalytic activity of the obtained photocatalysts, the photocatalytic hydrogen evolution from water splitting was carried out under visible-light irradiation (λ > 420 nm). For comparison, the two series of 3DOM-HxWO3/Pt/CdS with different molar ratio of CdS NPs loading and different H-treated temperature (25 °C to 250 °C) were also tested under the same conditions, respectively. As shown in Fig. S7, when the molar ratio of CdS:3DOM-HxWO3/Pt is 3:1 and H-treated temperature is at 100 °C, the as-prepared CHW100 sample shows the highest H2 evolution activity (Fig. 8a, 39.2 mmol g^{-1} h^{-1}, see video), which is 13.5 times than that of the pure CdS NPs (2.9 mmol g^{-1} h^{-1}) and infinitely fold than the HW100 (0 mmol g^{-1} h^{-1}). The result powerful proves that the formation of Z-scheme system can greatly enhance the hydrogen evolution. It should be noted that when the molar ratio of CdS:3DOM-HxWO3/Pt increased to 4:1, the photocatalytic activity of heterojunction sample has a notable decrease due to the shielding effect of excessive CdS NPs loading. In addition, when the 3DOM-HxWO3 was replaced by 3DOM-WO3, the 3DOM-WO3/Pt/CdS only has the half photocatalytic activity of CHW100 for the hydrogen production. This is because the main physicochemical properties of WO3, such as the light absorption, photoelectric properties and photon-generated charge carrier production ability, were worse than HxWO3. What's more, the reference sample of CdS/Pt (containing the same amount of Pt as 3DOM-HxWO3/Pt) shows almost unchanged HER activity in comparison with pure CdS. This is because the loading amount of Pt NPs on the CdS surface is too little to enhance the photocatalytic activity. From these above HER results, it can be deduced that the Pt NPs, in the system of 3DOM-HxWO3/Pt/CdS Z-scheme heterojunction, were mainly used to trigger the process of hydrogen spillover. In Fig. 8b, in order to investigate the stability of the as-formed photocatalysts, the cycling hydrogen evolution over the pure CdS and the CHW100 were tested. The photoactivity of pure CdS has an obvious decrease and just remains at 34% after five cycles for the hydrogen evolution. However, the CHW100 sample shows excellent photostability and its photoactivity remains at 90% after five consecutive cycles for 15 h reaction. These results conclusively reveal that Z-scheme heterojunction is a fascinating way to prevent the photocorrosion of CdS,

because the holes on surface of CdS can be timely and fast consumed by the electrons of 3DOM-HxWO3/Pt rather than oxidating the CdS [44,45].

Moreover, the apparent quantum efficiency of H2 evolution over the CdS and CHW100 samples was tested under different monochromatic incident lights. As listed in Table 1, the AQE of CdS for HER at 420 nm, 435 nm and 475 nm are 23.15%, 19.70% and 4.21%, respectively. As expected, the CHW100 sample shows much higher AQE of 58.80%, 53.75% and 18.55% at 420 nm, 435 and 475 nm, respectively, indicating that the construction of Z-scheme heterojunction through combining CdS with HxWO3 is greatly beneficial for the improvement of photocatalytic hydrogen evolution. In addition, it should be noted that in spite of the CHW100 material has excellent light absorption and photon-generated charge carrier production ability in Vis-NIR region (as show in Fig. 6b and Fig. S3.d–e), its AQE for HER at 550 nm still is zero. This is due to the fact that the CdS NPs with wide bandgap of 2.65 eV have no photoexcitation ability in the near infrared light region, and thus the unique Z-scheme charge transfer system cannot be formed in the CHW100 sample, leading to the neglectable charge separation efficiency.

3.3. Mechanism discussion

From the aforementioned analysis, it is clearly known that the construction of Z-scheme heterojunction via hydrogen spillover process can greatly enhance the HER activity due to the following structural advantage: (1) The formed HxWO3/Pt material would give birth to an amazing light absorption capacity and great charge carrier production ability under Vis-NIR light irradiation (as show in Fig. 2 and Fig. S3a-e). (2) The composite photocatalyst with large-scale three-dimensionally ordered macroporous structure can provide a lot of sites for the significant enhancement of mass transfer during the photoreaction. (3) By in-situ loading, the CdS nanoparticles can be uniformly grew on the surface of 3DOM-HxWO3 to form abundant charge transfer channels at the interface of Z-scheme heterojunction (Figs. 4d, 5 c and Fig. S6), as result of leading to excellent charge transport efficiency in the 3DOM-HxWO3/Pt/CdS sample (Fig. 6).

In order to better understand the possible photocatalytic reaction mechanism of hydrogen evolution in the presence of 3DOM-HxWO3/Pt/CdS, a charge transfer route at the interface of the as-prepared heterojunction sample was proposed and the schematic diagram is illustrated in Fig. 9. As shown in Fig. 9a, when the solar light begins to irradiate the 3DOM-HxWO3 sample, numerous electron-hole pairs are firstly generated in the valence band (VB) of HxWO3. These electrons (e^-_{HxWO3}) can fast transfer to its conduct band (CB), while the holes (h^+_{HxWO3}) remain on its valence band. At the same time, the CdS NPs similarly produce numerous electron-hole pairs as long as the wavelength of the irradiation light is shortened than 500 nm. According to Z-scheme charge transfer mechanism, the holes on the VB of CdS are constantly captured by the electrons which came from the CB of 3DOM-HxWO3 (Eq. (2) in Fig. 9b). In the meanwhile, the holes on the VB of 3DOM-HxWO3 were consumed by the scavenger of lactic acid (Eq. (3) in Fig. 9b). Finally, the remaining electrons on the CB of CdS would react with H$^+$ to produce hydrogen rather than transfer into the CB of HxWO3 (Eq. (1) in Fig. 9b), because if they do, this material of 3DOM-HxWO3/Pt/CdS would lose the ability to produce the H2.

4. Conclusions

The novel 3DOM-HxWO3/Pt/CdS Z-scheme heterojunctions have been well designed and prepared via the hydrogen spillover combined with in-situ hydrothermal method. In this composite photocatalyst, the degree of hydrogen-doping can be artificial tuned via the careful change of hydrogen spillover temperature. When the H-treated temperature reached to 100 °C, the 3DOM-HxWO3/Pt (HW100 sample) exhibits high visible light absorption, ultrahigh electron conductivity and

excellent charges excitation ability. In addition, the HxWO₃ with three-dimensionally ordered macroporous structure could provide a lot of active sites for the growth of CdS NPs, leading to the formation of special Z-scheme charge transfer system at the interface between HxWO₃ and CdS, which thus endow the 3DOM-HxWO₃/Pt/CdS photocatalyst with great charge separation efficiency as well as long electron lifetime. As a result, the CHW_{100} sample shows an excellent hydrogen evolution (39.2 mmol $g^{-1} h^{-1}$) and high AQE (58.80%), which displays a good engineering application potential.

Acknowledgements

Appendix A. Supplementary data

Supplementary material related to this article can be found, in the online version, at doi:https://doi.org/10.1016/j.apcatb.2019.117812.

References

[1] N.Q. Tran, V.Q. Bui, H.M. Le, Y. Kawazoe, H. Lee, Anion–cation double substitution in transition metal dichalcogenide to accelerate water dissociation kinetic for electrocatalysis, Adv. Energy Mater. (2018) 1702139–1702148.

[2] Z.H. Xiao, Y. Wang, Y.C. Huang, Z.X. Wei, C.L. Dong, J.M. Ma, S.H. Shen, Y.F. Li, S.Y. Wang, Filling the oxygen vacancies in Co₃O₄ with phosphorus: an ultra-efficient electrocatalyst for overall water splitting, Energy Environ. Sci. 10 (2017) 2563–2569.

[3] J. Zhang, J. Yu, Y.M. Zhang, Q. Li, J.R. Gong, Visible light photocatalytic H₂-production activity of CuS/ZnS porous nanosheets based on photoinduced interfacial charge transfer, Nano Lett. 11 (2011) 4774–4779.

[4] F.R. Lucci, M.D. Marcinkowski, T.J. Lawton, E.C.H. Sykes, H₂ Activation and spillover on catalytically relevant Pt–Cu single atom alloys, J. Phys. Chem. C 119 (2015) 24351–24357.

[5] G.G. Zhang, Z.A. Lan, X.C. Wang, Surface engineering of graphitic carbon nitride polymers with cocatalysts for photocatalytic overall water splitting, Chem. Sci. 8 (2017) 5261–5274.

[6] H. Tabassum, W.H. Guo, W. Meng, A. Mahmood, R. Zhao, Q.F. Wang, R.Q. Zou, Metal–organic frameworks derived cobalt phosphide architecture encapsulated into B/N Co-doped graphene nanotubes for all pH value electrochemical hydrogen evolution, Adv. Energy Mater. 7 (2017) 1601671–1601677.

[7] J.Y. Li, M. Yan, X.M. Zhou, Z.Q. Huang, Z.M. Xia, C.R. Chang, Y.Y. Ma, Y.Q. Qu, Mechanistic insights on ternary Ni₂₋ₓCoₓP for hydrogen evolution and their hybrids with graphene as highly efficient and robust catalysts for overall water splitting, Adv. Funct. Mater. 26 (2016) 6785–6796.

[8] L. Wei, T.S. Zhao, Q. Xu, X.L. Zhou, Z.H. Zhang, In-situ investigation of hydrogen evolution behavior in vanadium redox flow batteries, Appl. Energy 190 (2017) 1112–1118.

[9] R. Shi, H.F. Ye, F. Liang, Z. Wang, K. Li, Y.X. Weng, Z.S. Lin, W.F. Fu, C.M. Che, Y. Chen, Interstitial P-doped CdS with long-lived photogenerated electrons for photocatalytic water splitting without sacrificial agents, Adv. Mater. 30 (2018) 1705941–1705946.

[10] H. Li, X.Q. Yan, B. Lin, M.Y. Xia, J.J. Wei, B.L. Yang, G.D. Yang, Controllable spatial effect acting on photo-induced CdS@CoP@SiO₂ ball-in-ball nano-photoreactor for enhancing hydrogen evolution, Nano Energy 47 (2018) 481–493.

[11] J. Liu, Y. Liu, N.Y. Liu, Y.Z. Han, X. Zhang, H. Huang, Y. Lifshitz, S.T. Lee, J. Zhong, Z.H. Kang, Metal-free efficient photocatalyst for stable visible water splitting via a two-electron pathway, Science 347 (2015) 970–974.

[12] L. Zhang, W.Z. Wang, S.M. Sun, D. Jiang, Near-infrared light photocatalysis with metallic/semiconducting HxWO₃/WO₃ nanoheterostructure in situ formed in mesoporous template, Appl. Catal. B: Environ. 168 (2015) 9–13.

[13] A. Hjelm, C.G. Granqvist, J.M. Wills, Electronic structure and optical properties of WO₃, LiWO₃, NaWO₃, and HWO₃, Phys. Rev. B 54 (1996) 2436–2445.

[14] Y.J. Xi, Q.F. Zhang, H.S. Cheng, Mechanism of Hydrogen Spillover on WO₃ (001) and Formation of HₓWO₃ (x = 0.125, 0.25, 0.375, and 0.5), J. Phys. Chem. C 118 (2013) 494–501.

[15] H.F. Cheng, M.C. Wen, X.C. Ma, Y. Kuwahara, K. Mori, Y. Dai, B.B. Huang,
H. Yamashita, Hydrogen doped metal oxide semiconductors with exceptional and tunable localized surface plasmon resonances, J. Am. Chem. Soc. 138 (2016) 9316–9324.

[16] C.S. Guo, S. Yin, L.J. Huang, T. Sato, Synthesis of one-dimensional potassium tungsten bronze with excellent near-infrared absorption property, ACS Appl. Mater. Interfaces 3 (2011) 2794–2799.

[17] Z.G. Zhao, M. Miyauchi, Nanoporous-walled tungsten oxide nanotubes as highly active visible-light-driven photocatalysts, Angew. Chem. Int. Ed. 47 (2008) 7051–7055.

[18] J.C. Wang, H.C. Yao, Z.Y. Fan, L. Zhang, J.S. Wang, S.Q. Zang, Z.J. Li, Indirect Z-scheme BiOI/g-C₃N₄ photocatalysts with enhanced photoreduction CO₂ activity under visible light irradiation, ACS. Appl. Mater. Inter. 8 (2016) 3765–3775.

[19] F.Q. Zhou, J.C. Fan, Q.J. Xu, Y.L. Min, BiVO₄ nanowires decorated with CdS nanoparticles as Z-scheme photocatalyst with enhanced H₂ generation, Appl. Catal. B: Environ. 201 (2017) 77–83.

[20] Q.Y. Li, G.R. Duan, J. Luo, X.H. Liu, Ultrasonic-assisted synthesis of plasmonic Z-scheme Ag/AgCl/WO₃-nanoflakes photocatalyst in geothermal water with enhanced visible-light photocatalytic performance, J. Energy. Chem. 27 (2017) 826–835.

[21] X.Q. Yan, M.Y. Xia, B.R. Xu, J.J. Wei, B.L. Yang, G.D. Yang, Fabrication of novel all-solid-state Z-scheme heterojunctions of 3DOM-WO₃/Pt coated by mono-or few-layered WS₂ for efficient photocatalytic decomposition performance in Vis-NIR region, Appl. Catal. B: Environ. 232 (2018) 481–491.

[22] O. Arutanti, A.F. Arif, R. Balgis, T. Ogi, K. Okuyama, Tailored synthesis of macroporous Pt/WO₃ photocatalyst with nanoaggregates via flame assisted spray pyrolysis, AIChE. J. 62 (2016) 3864–3873.

[23] M.C. Chang, Three dimensionally ordered microstructure of polycrystalline TiO₂ ceramics with micro/meso Porosity, J. Korean Ceram. Soc. 53 (2016) 227–233.

[24] G. Lui, G. Li, X.L. Wang, G.P. Jiang, E. Lin, M. Fowler, A. Yu, Z.W. Chen, Flexible, three-dimensional ordered macroporous TiO₂ electrode with enhanced electrode–electrolyte interaction in high-power Li-ion batteries, Nano Energy 24 (2016) 72–77.

[25] X.Q. Yan, C. Xue, B.L. Yang, G.D. Yang, Novel three-dimensionally ordered macroporous Fe³⁺-doped TiO₂ photocatalysts for H₂ production and degradation applications, Appl. Surf. Sci. 394 (2017) 248–257.

[26] L. Ernawati, T. Ogi, R. Balgis, K. Okuyama, M. Stucki, S.C. Hess, W.J. Stark, Hollow silica as an optically transparent and thermally insulating polymer additive, Langmuir 32 (2015) 338–345.

[27] A.G. Dong, Y.J. Wang, Y. Tang, N. Ren, W.L. Yang, Z. Gao, Fabrication of compact silver nanoshells on polystyrene spheres through electrostatic attraction, Chem. Commun. 4 (2002) 350–351.

[28] C.Mi Ding, J.Y. Shi, D.E. Wang, Z.J. Wang, N. Wang, G.J. Liu, F.Q. Xiong, C. Li, Visible light driven overall water splitting using cocatalyst/BiVO4 photoanode with minimized bias, Phys. Chem. Chem. Phys. 15 (2013) 4589–4595.

[29] C.H. Chang, Y.L. Lee, Chemical bath deposition of CdS quantum dots onto mesoscopic TiO₂ films for application in quantum-dot-sensitized solar cells, Appl. Phys. Lett. 91 (2007) 053503–053506.

[30] I. Robel, V. Subramanian, M. Kuno, P.V. Kamat, Quantum dot solar cells. Harvesting light energy with CdSe nanocrystals molecularly linked to mesoscopic TiO₂ films, J. Am. Chem. Soc. 128 (2006) 2385–2393.

[31] Y.J. Shen, Y.L. Lee, Y.M. Yang, Monolayer behavior and langmuir− blodgett manipulation of CdS quantum dots, J. Phys. Chem. B 110 (2006) 9556–9564.

[32] B. Lin, H. Li, H. An, W.B. Hao, J.J. Wei, Y.Z. Dai, C.S. Ma, G.D. Yang, Appl. Catal. B: Environ. 220 (2018) 542–552.

[33] X.Q. Yan, K. Ye, T.X. Zhang, C. Xue, D. Zhang, C.S. Ma, J.J. Wei, G.D. Yang, Formation of three-dimensionally ordered macroporous TiO₂@nanosheet SnS₂ heterojunctions for exceptional visible-light driven photocatalytic activity, New J. Chem. 41 (2017) 8482–8489.

[34] D.Z. Lu, H.M. Wang, X.N. Zhao, K.K. Kondamareddy, J.Q. Ding, C.H. Li, P.F. Fang, Highly efficient visible-light-induced photoactivity of Z-scheme g-C₃N₄/Ag/MoS₂ ternary photocatalysts for organic pollutant degradation and production of hydrogen, ACS Sustain. Chem. Eng. 5 (2017) 1436–1445.

[35] J.S. Lu, J.J. Wang, F. Liu, L. Zhang, S.N. Chai, Fabrication of a direct Z-scheme type WO₃/Ag₃PO₄ composite photocatalyst with enhanced visible-light photocatalytic performances, Appl. Surf. Sci. 393 (2017) 180–190.

[36] G.M. Wang, Y.C. Ling, H.Y. Wang, X.Y. Yang, C.C. Wang, J.Z. Zhang, Y. Li, Hydrogen-treated WO₃ nanoflakes show enhanced photostability, Energy Environ. Sci. 5 (2012) 6180–6187.

[37] L. Bartha, A.B. Kiss, T. Szalay, Chemistry of tungsten oxide bronzes, Int. J. Refract. Met. H 13 (1995) 77–91.

[38] F.J. Castro, F. Tonus, J.L. Bobet, G. Urretavizcaya, Synthesis of hydrogen tungsten bronzes HxWO₃ by reactive mechanical milling of hexagonal WO₃, J. Alloy Compd. 495 (2010) 537–540.

[39] Y. Feldman, E. Wasserman, D.J. Srolovitz, R. Tenne, High-rate, gas-phase growth of MoS₂ nested inorganic fullerenes and nanotubes, Science 267 (1995) 222–225.

[40] L.C. Wang, Y. Wang, Y. Cheng, Z.F. Liu, Q.S. Guo, M.N. Ha, Z. Zhao, Hydrogen-treated mesoporous WO₃ as a reducingagent of CO₂ to fuels (CH₄ and CH₃OH) with enhanced photothermal catalytic performance, J. Mater. Chem. A 4 (2016) 5314–5322.

[41] F.Y. Xie, L. Gong, X. Liu, Y.T. Tao, W.H. Zhang, S.H. Chen, H. Meng, J. Chen, XPS studies on surface reduction of tungsten oxide nanowire film by Ar⁺ bombardment, J. Electron Spectrosc. Relat. Phenom. 185 (2012) 112–118.

[42] D.C. Jiang, Z.J. Sun, H.X. Jia, D.P. Lu, P.W. Du, A cocatalyst-free CdS nanorod ZnS nanoparticle composite for high-performance visible-light-driven hydrogen production from water, J. Mater. Chem. A 4 (2016) 675–683.

[43] J.Y. Zhang, Y.H. Wang, J. Jin, J. Zhang, Z. Lin, F. Huang, J.G. Yu, Efficient visible-

light photocatalytic hydrogen evolution and enhanced photostability of core/shell CdS/g-C$_3$N$_4$ nanowires, ACS Appl. Mater. Interfaces 5 (2013) 10317–10324.

[44] C. Xue, X.Q. Yan, H. An, H. Li, J.J. Wei, G.D. Yang, Bonding CdS-Sn$_2$S$_3$ eutectic clusters on graphene nanosheets with unusually photoreaction-driven structural reconfiguration effect for excellent H2 evolution and Cr (VI) reduction, Appl. Catal.

B: Environ. 222 (2018) 157–166.

[45] F.K. Ma, Y.Z. Wu, Y.L. Shao, Y.Y. Zhong, J.X. Lv, X.P. Hao, 0D2D nanocomposite visible light photocatalyst for highly stable and efficient hydrogen generation via recrystallization of CdS on MoS$_2$ nanosheets, Nano Energy 27 (2016) 466–474.